Terdiurnal Radiational Tides

R. D. Ray,[a] J.-P. Boy,[b] S. Y. Erofeeva,[c] and G. D. Egbert[c]

[a] *Geodesy & Geophysics Lab., NASA Goddard Space Flight Center, Greenbelt, Maryland*

[b] *EOST, Université de Strasbourg, Strasbourg, France*

[c] *College of Earth, Ocean, & Atmospheric Sciences, Oregon State University, Corvallis, Oregon*

Corresponding author: R. D. Ray, richard.ray@nasa.gov

ABSTRACT: Terdiurnal atmospheric tides induce an S_3 radiational ocean tide, similar to radiational tides S_1 and S_2 in the diurnal and semidiurnal bands. Although of small amplitude, the terdiurnal tide has some intriguing properties. The tide has an unusually pronounced seasonal variation, manifested by annual sidelines here denoted R_3 and T_3, which causes the tide to nearly vanish during times near an equinox. Forcing is generally largest in the winter hemisphere. Complicating matters, the two sideline frequencies coincide with those of nonlinear compound tides SK_3 and SP_3. Whether radiational tides or nonlinear tides (or both) are appearing at any given tide gauge can usually be determined by the relative amplitudes and phase differences of the two sidelines. The amplitudes of R_3 and T_3 are generally comparable; the amplitudes of SK_3 and SP_3 are not. Proper identification can lead to a small improvement in tidal prediction, but more importantly can lead to improved physical interpretation. An example from recent measurements under the Ross Ice Shelf bears on the role of nonlinearity in interactions between the ocean tide and the floating ice shelf.

1. Introduction

"Radiational tides," a term that harkens back to Munk and Cartwright (1966), refers to those tidal constituents—or components of constituents—that are forced ultimately by solar radiation rather than by the gravitational tidal potential. Although there was some early confusion about what this meant (Godin 1986), it is now clear that the proximate driver of radiational ocean tides is loading by atmospheric pressure tides, which are themselves generated by insolation. These points have been well established by detailed analyses and modeling of radiational tides in the semidiurnal tidal band (Zetler 1971; Arbic 2005; Dobslaw and Thomas 2005) and the diurnal band (Ray and Egbert 2004; Lyard et al. 2006). The major semidiurnal constituent S_2 is, very roughly, 80% gravitational and 20% radiational; the diurnal S_1 is reversed, perhaps 90% radiational and only 10% gravitational, again very roughly. In each case the partitioning can be fairly accurately determined because the gravitational contribution can be inferred from major constituents at nearby frequencies—K_2 in the case of the semidiurnal band, K_1 and P_1 in the diurnal.

This paper examines radiational tides in the terdiurnal band, nominally at the frequency of S_3, or 3 cycles per solar day (cpd). Like terdiurnal tides everywhere, these tides are small, rarely more than a few mm amplitude, so they often escape notice. The terdiurnal radiational tides are nonetheless so unusual and intriguing—and indeed their forcing almost bizarre—that an in-depth study of them can hardly be resisted despite their small size.

In contrast to the diurnal and semidiurnal bands, there is no gravitational forcing of solar tides in the terdiurnal band, since the sun's parallax is so small. Thus, there is no entangling of gravitational and radiational effects for S_3 as there is for S_1 and especially for S_2. There are, however, other complications. As we show in Section 3 the S_3 barometric tide has an unusually large seasonal modulation. In fact, the two seasonal sidelines of S_3, with frequencies ± 1 cycles/year (cpy) from the central S_3 line, are often larger than the central line itself. An example, from barometer measurements taken at Hilo, Hawaii, is shown in Figure 1. Attention must therefore focus on the two sidelines as well as on S_3, and it so happens that in the ocean the two sidelines coincide in frequency with two nonlinear compound tides, SK_3 and SP_3, which are nominally the result of nonlinear interaction between S_2 and the diurnal constituents K_1 and P_1, respectively. So there is still entanglement, but this time between effects of nonlinearity and insolation. Both effects are found to be important; quite often one effect dominates in some ocean regions, and the other in

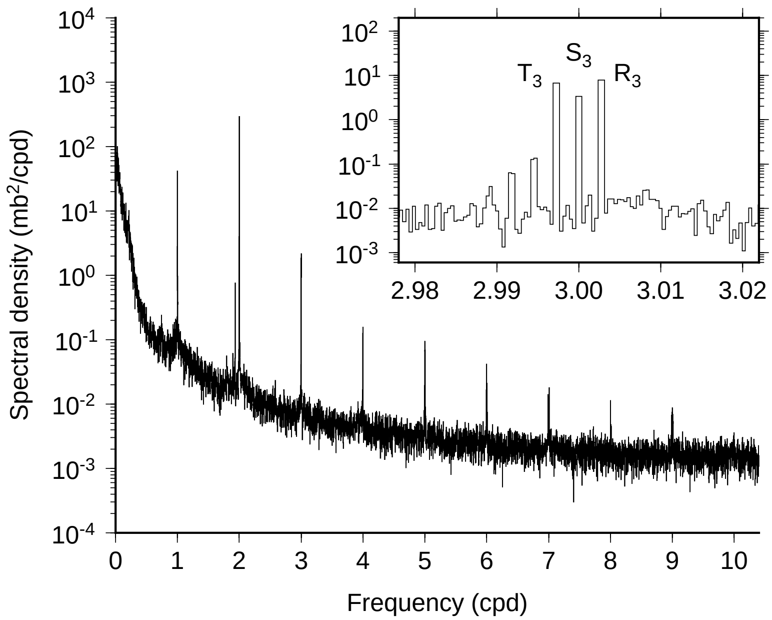

FIG. 1. Spectrum of observed barometric pressure at Hilo, Hawaii, based on a 14-year time series (1982–1995). Inset is a zoom view of the terdiurnal band, showing S_3 and its two annual sidelines, here called T_3 and R_3, which are both larger than the central peak. There are also very small peaks to the left of T_3, indicating some coherent intra-annual variability. In the full spectrum, small lunar atmospheric tides are noticeable just to the left of the dominant S_2 peak.

other regions. Distinguishing between the two is clearly necessary if any attempt is made to model these waves or even to understand measurements of them.

There are other reasons that warrant distinguishing nonlinear from radiational causes. One practical reason arises from tidal prediction, where proper identification leads to a small improvement, as discussed in Section 6a. An interesting physical application involves the ocean tide's interaction with the Ross Ice Shelf, where ice-shelf motion may appear at frequencies usually associated with nonlinearity, and it is then important to understand whether the ocean tide is also nonlinear or only the ice shelf's response is nonlinear. This is discussed in Section 6b. These discussions are preceded by some preliminaries, with Section 3 devoted to examination of the S_3 air tide and Sections 4 and 5 devoted to the ocean tide. An appendix gives further details concerning our knowledge of the relevant air tides.

Table 1. Tidal constituents in the terdiurnal S_3 group.*

Tide	Frequency (deg/hour)	Source	Nodal modulation?	Argument
SP_3	44.958931	Nonlinear	Small	$3T - h - \pi/2$
T_3	44.958931	Radiational	None	$3T - h + \pi$
S_3	45.000000	Radiational	None	$3T + \pi$
R_3	45.041069	Radiational	None	$3T + h + \pi$
SK_3	45.041069	Nonlinear	Large	$3T + h + \pi/2$

* T is Universal Time; h is the mean longitude of the sun.

2. The S_3 tidal group

We find it advantageous to adopt a tidal nomenclature to distinguish the nonlinear tides from the radiational tides. For the annual sidelines of the S_3 atmospheric tide, as well as the corresponding ocean response, it seems inappropriate to employ standard names of compound tides SK_3 and SP_3. Following Kelvin's convention in the semidiurnal band of adopting alphabetical neighbors—thus, R_2 and T_2 are the annual sidelines of S_2—we adopt R_3 and T_3 as the annual sidelines to a purely radiational S_3. The arguments of the sidelines differ from the S_3 argument by $\pm h$, where h is the mean longitude of the sun, with period of one tropical year. A formula for h sufficiently accurate for the late twentieth and early twenty-first centuries is (Meeus 1998)

$$h = 280.466^\circ + 0.985647^\circ T_d$$

where T_d is the number of days since 12:00 UTC 1 January 2000. The tides of interest here are summarized in Table 1, where the arguments assume standard use of cosine functions.

There is one important difference with Kelvin's semidiurnal arguments. Because the annual modulation of the gravitational S_2 is caused by the annual variation in the distance between sun and earth, the time dependences of R_2 and T_2 are relative to perihelion and their arguments thus include p_s, the mean longitude of perihelion relative to the equinox (e.g., Pugh and Woodworth 2014). In contrast, the primary annual modulation of the radiational S_3 is caused by the climatic effects of the sun's varying declination, and the solar distance is secondary Thus, our arguments of R_3 and T_3 do *not* include p_s. (In Table 1 the phase offsets of $\pm\pi/2$ for SK_3 and SP_3 carry forward from the arguments of the interacting constituents K_1 and P_1, but the offset of $+\pi$ in the radiational constituents is less justified and in fact was not used by Ray and Poulose (2005). The extra π in S_3, however, is consistent with the conventions of the International Hydrographic Organization,[1] so we have here followed that convention; the extra π in the sidelines then follows so that their arguments differ by exactly $\pm h$ from the central line.)

Note that SK_3 has a significant 18.6-y nodal modulation, arising mostly from the interacting K_1 constituent; it amounts to about ±12% in amplitude and ±9° in phase (Pugh and Woodworth 2014). The radiational R_3 has none. This difference can have a minor effect on tidal prediction (Section 6a).

In tidal analysis of a short time series, the three constituents of the S_3 group may not be separable. Nominally 6 months of observations are needed to separate the two sidelines, and 12 months are needed to separate all three frequencies. When a short series is analyzed, most software packages solve for a single constituent, assuming it to be SK_3.

3. Terdiurnal barometric tides

A quantitative understanding of the ocean's response to terdiurnal atmospheric loading requires a model of the terdiurnal barometric tides. Analyses of individual time series of barometric pressure, as in Figure 1, are invaluable as a guide, but island meteorological stations are too sparse to allow us to develop reliable global charts. As with diurnal and semidiurnal tides (e.g., Covey et al. 2014; Dobslaw and Thomas 2005), it is beneficial to extract terdiurnal signals from the global pressure products of numerical weather models. Data from island stations can then act as "ground truth" for these results (which is done below in Appendix A). We used hourly surface pressures from the European Centre for Medium-Range Weather Forecasts (ECMWF) ERA5 reanalysis (Hersbach et al. 2020). The hourly time-stepping nowadays available in products like ERA5 is more than adequate for tidal studies, including signals in the terdiurnal band, and this considerably simplifies tidal inversions compared with approaches needed to handle older 6-hourly sampling (van den Dool et al. 1997). Our ERA5 data covered the time span 2000–2017. Tidal solutions for the three harmonics S_3, R_3, and T_3 are shown in Figure 2.

For comparison we have also computed the same fields from the Modern-Era Retrospective Analysis for Research and Applications, version 2 (MERRA-2), produced by the NASA Global Modeling and Assimilation Office (Gelaro et al. 2017). These are also hourly surface pressures

[1]IHO Committee for Tides, Water Level and Currents at `https://iho.int/en/twcwg`

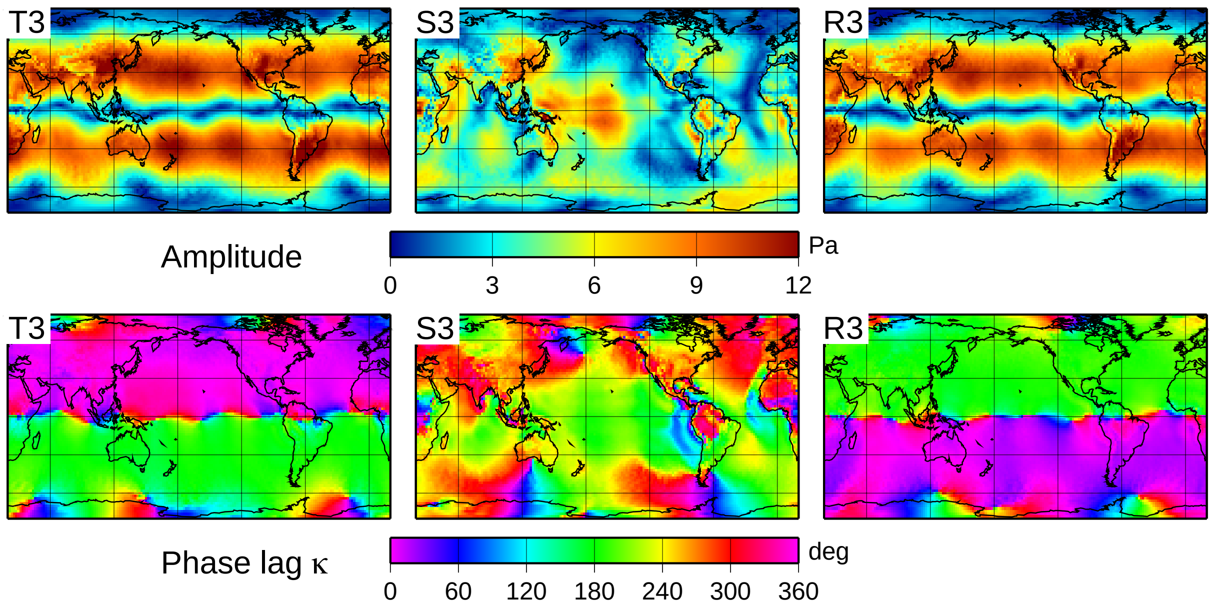

FIG. 2. Amplitudes (top) and phase lags (bottom) of three terdiurnal atmospheric surface-pressure tides as extracted from ERA5 reanalysis. The phase lags κ are relative to local (not Greenwich) transit of the sun.

and covered the period 1980–2017. The results are qualitatively similar to those of Figure 2 for T_3 and R_3, but not for the small S_3 constituent where the patterns are quite different. Tests described in Appendix A suggest that the ERA5 solutions are to be preferred.

According to Figure 2, the two sidelines R_3 and T_3 are of comparable amplitudes, and they are almost everywhere larger than the central S_3 line. This agrees with the Hilo spectrum (Figure 1) as well as results obtained at 180 barometer stations spread across the continental United States (Ray and Poulose 2005). Near the equator, however, the amplitudes of both sidelines are nearly zero as the phases flip 180°. Aside from being smaller, S_3 displays features that appear tied to local geography (not zonally symmetric) presumably reflecting non-migrating, localized boundary heating.

Although we solved for Greenwich phase lags G, following usual oceanographic approaches (Pugh and Woodworth 2014), it is more enlightening for Figure 2 to use local phase lags κ, given by (Schureman 1940, p. 77)

$$\kappa = G + m\lambda,$$

where λ is longitude in degrees east and m is the species number (3 for terdiurnals). In terms of κ, the phases of T_3 and R_3 are seen to be nearly constant but with northern and southern hemispheres 180° different.

The implications of two sidelines of comparable amplitude but flipped in phase is brought out more clearly by combining the three terdiurnal constituents into a single time-varying terdiurnal tide whose amplitude and phase varies throughout the year (parameterized most easily as a function of the solar longitude h). Combining the three arguments of Table 1 into a single modulated wave that varies with h is an exercise in simple trigonometry. The result, evaluated at the March equinox, June solstice, September equinox, and December solstice (i.e., at h =0°, 90°, 180°, 270°, respectively), is shown in Figure 3. For the two solstice seasons we also show the phase, in terms of the local time (modulo 8 hours) of maximum pressure.

As Figure 3 shows, the terdiurnal atmospheric tide almost completely disappears during both equinox seasons. It peaks (in mid-latitudes) during the solstice seasons, with the amplitudes largest in wintertime for both northern and southern hemispheres. During those peak seasons, the (local) phase is nearly constant across each hemisphere, with the tide peaking near 2:00 in winter and near 6:00 in summer (again modulo 8 h).

Studies of the terdiurnal air tide in the early (Hann 1918) and middle (Siebert 1961) twentieth century made note of the unusual aspects displayed in Figure 3, including the phase asymmetry between north and south and between summer and winter, and the wave's disappearance during each equinox. These properties of the terdiurnal tide are hardly mentioned in the modern literature. Most modern studies focus on the upper atmosphere, where terdiurnal oscillations in wind speed (Smith 2000) and temperature (Moudden and Forbes 2013) are a pronounced feature of subdiurnal variability, with magnitudes in some places even comparable to the diurnal wave (Thayaparan 1997). Like the barometric tide, the tide in the mesosphere and lower thermosphere is generally largest in winter, but it does not vanish during equinox seasons (e.g. Akmaev 2001; Moudden and Forbes 2013).

4. Ocean observations

Before examining the ocean's response to loading by the terdiurnal atmospheric tides—the topic of Section 5—it is useful to examine some ocean observations. As noted in the Introduction and

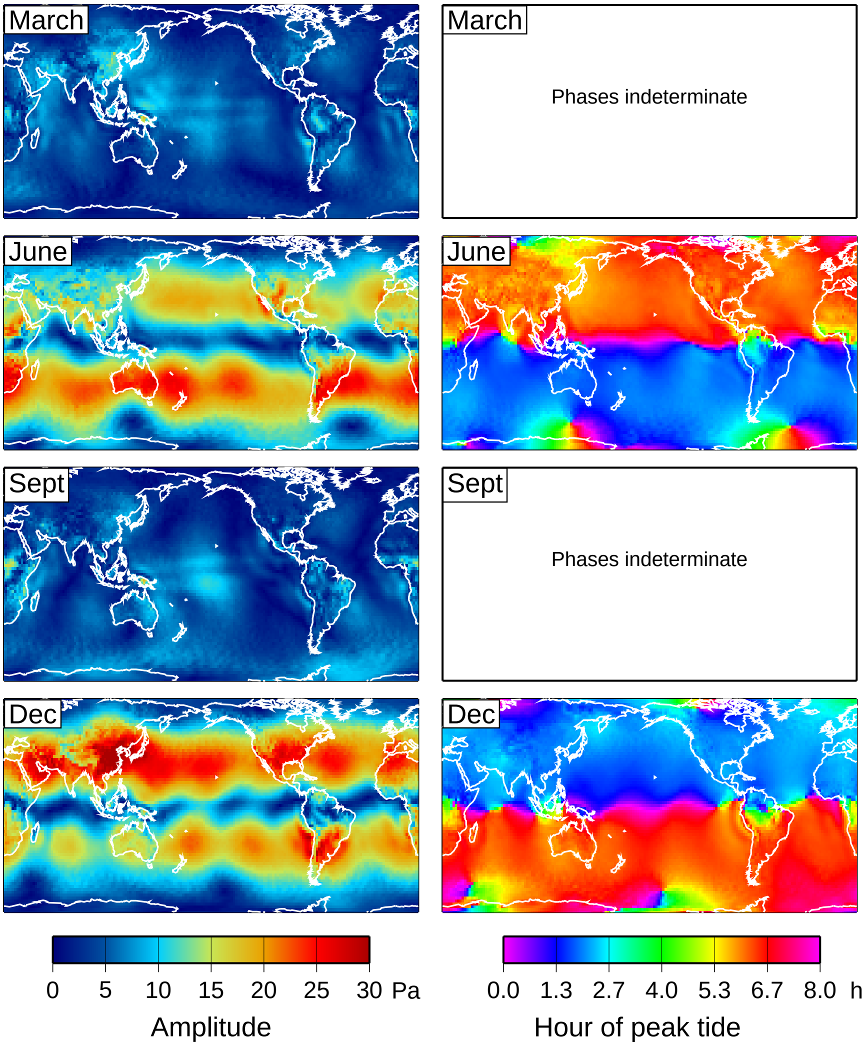

FIG. 3. Amplitudes (left) and phases (right) of the terdiurnal atmospheric tide in each season, evaluated by combining the three constituents T_3, S_3, R_3 into a single time-varying tide. Phases are in terms of local time of maximum pressure; they are not shown for the equinox seasons when they become indeterminate owing to vanishing amplitudes. Largest amplitudes occur in middle latitudes during winter, for each hemisphere, while nearly-constant hemispheric phases flip at the equinoxes.

in Section 2, the S_3 group contains the two nonlinear compound constituents, SK_3 and SP_3. In tidal analysis of tide gauge data, amplitudes at these two frequencies are often observed to be the largest, or nearly the largest, in the whole terdiurnal band, which is a surprising fact—if the tides are truly compound tides—since the compound constituents MK_3 and MO_3 should generally be larger owing to the generally larger principal tide M_2. As the reader must suspect, SK_3 and SP_3

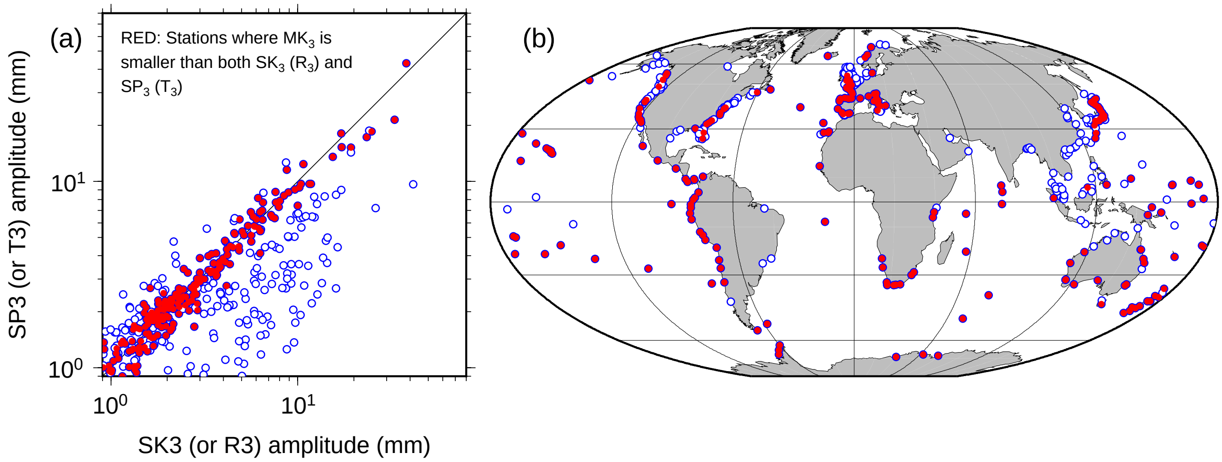

FIG. 4. **(a)** Comparisons of SK_3 and SP_3 amplitudes (or equivalently R_3 and T_3 amplitudes) estimated from 515 tide-gauge time series. Red dots are locations where the amplitude of MK_3 is smaller than both SK_3 and SP_3, thus indicating minimal nonlinearity (typically MK_3 is the largest nonlinear tide in the terdiurnal band). For red dots, radiational effects therefore dominate the S_3 tidal group. White dots below the diagonal are likely dominated by nonlinear effects; white dots near or above the line are about equally affected by nonlinear and radiational forcing. **(b)** Locations of the 515 tide gauges.

are often large because they are in reality the radiational tides T_3 and R_3, or some combination of compound and radiational tides.

To examine this more closely we have undertaken tidal analyses of data from the GESLA2 database of hourly (or more rapid) tide gauge measurements compiled by Woodworth et al. (2017). Of the original 1274 time series, we have discarded duplicates, series shorter than 8 full years, and stations located far up rivers (e.g., Philadelphia), to arrive at 553 time series. We discarded another 38 stations where the standard errors of SK_3 or MK_3 were larger than their amplitudes. Locations of the remaining 515 stations are shown in Figure 4b.

For each station we compared the amplitudes of the three constituents SK_3 (or equivalently R_3), SP_3 (or equivalently T_3), and MK_3, the first two via a ‘scatter plot’ shown in Figure 4a. In about half the 515 stations (238), MK_3 has the largest amplitude of the three constituents. These are locations where nonlinearity is evidently significant. In the other half (245), MK_3 is found to have the smallest amplitude. Nonlinearity is less important at these locations, which are denoted by red dots in Figure 4. The interesting point is that these stations show approximately equal amplitudes for SP_3 and SK_3, with red dots falling along the diagonal of panel (a), which is what may be expected based on the approximately equal amplitudes of the two seasonal sidelines of the terdiurnal air tide. Thus, red dots in panel (a) are likely locations where the S_3 group is dominated by radiational forcing. Open dots below the diagonal are likely dominated by nonlinearity, with SK_3 of greater amplitude than SP_3, as the K_1 constituent is always of greater amplitude than P_1. For open dots near (or above) the diagonal, the S_3 group is likely a combination of both nonlinear and radiational effects.

Evidently an initial indicator of whether one is dealing with radiational T_3 and R_3 or nonlinear SP_3 and SK_3 is the relative amplitudes of the two lines. If the two are comparable, especially if MK_3 is small, then they are surely radiational. If the higher frequency line dominates, especially when MK_3 is significant, then they are surely compound tides. Many tide gauges, of course, will reflect a mixture of both effects.

In the deep open ocean, nonlinear effects are expected to be relatively small. For this regime we have examined a set of 71 bottom-pressure stations where the terdiurnal tides have been estimated. This is a subset of a previously constructed set of 151 stations (Ray 2013), not all of which could be used for various reasons. (For example, at some stations harmonic constants were derived by other investigators and did not include terdiurnal tides; some time series were too short to separate the constituents of interest.) Figure 5a, following Figure 4, compares amplitudes of the two sidelines, and it indicates generally comparable amplitudes, suggesting that these are mainly radiational tides. Even for those few cases where MK_3 is larger than at least one of the sidelines, the dots remain close to the line of unit slope. We conclude that throughout most of the open ocean, it is likely that energy in the S_3 tidal group is arising from radiational forcing, and that R_3, T_3 are in play rather than the nonlinear constituents SP_3, SK_3.

5. Ocean response to radiational forcing

To model the terdiurnal radiational ocean tides, we employed the forward-modeling capabilities of the OTIS (Oregon Tidal Inversion Software) package, solving the linearized shallow water equations by direct matrix factorization (Egbert and Erofeeva 2002), but without data assimilation. The air-pressure tides from ERA5, described in Section 3, were used as forcing. We used a global $(1/6)^\circ$ grid. Ocean self-attraction and crustal loading were included via an iterative procedure.

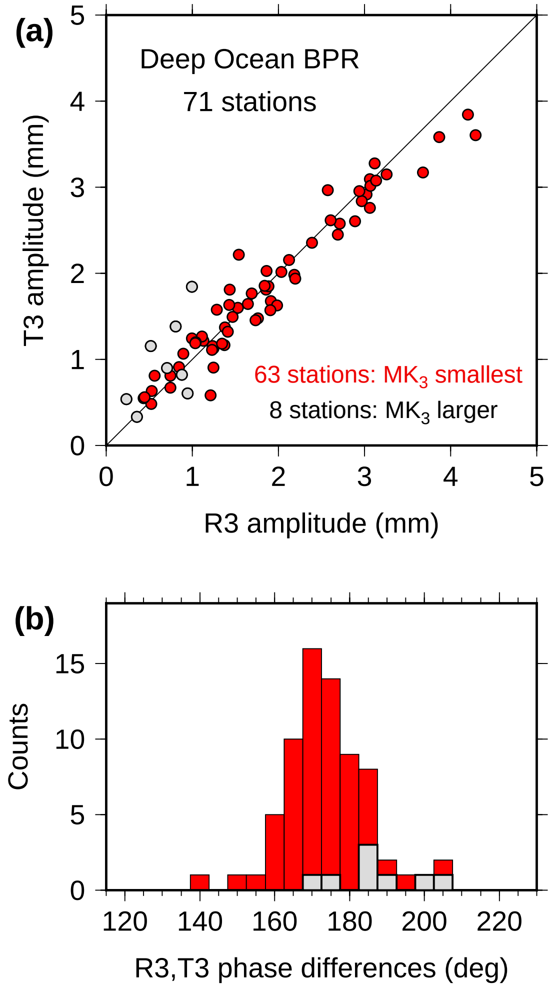

FIG. 5. (a) As in Figure 4a, but for 71 bottom-pressure stations where nonlinear tidal effects may be expected to be minimal. Red dots are stations where the nonlinear compound constituent MK_3 is smaller than both R_3 (or SK_3) and T_3 (or SP_3). (b) Histogram of phase differences between R_3 and T_3 tides. Phase differences cluster around 180°, in keeping with the air-tide phase differences (Figure 2).

When using direct matrix factorization, OTIS implements a linearized bottom friction, ru, with proportionality constant $r = C_D|U_b|$, where the drag coefficient $C_D = 0.003$ and U_b is considered a "background velocity," which can be constant or variable. It is generally useful to set U_b to values somewhat larger than realistic tidal velocities. We experimented with a range of U_b values, comparing against in situ data (see below) and ended by selecting a constant $U_b = 3$ m s^{-1}, or $r = 0.01$ m s^{-1}; but in no sense is this an optimal value.

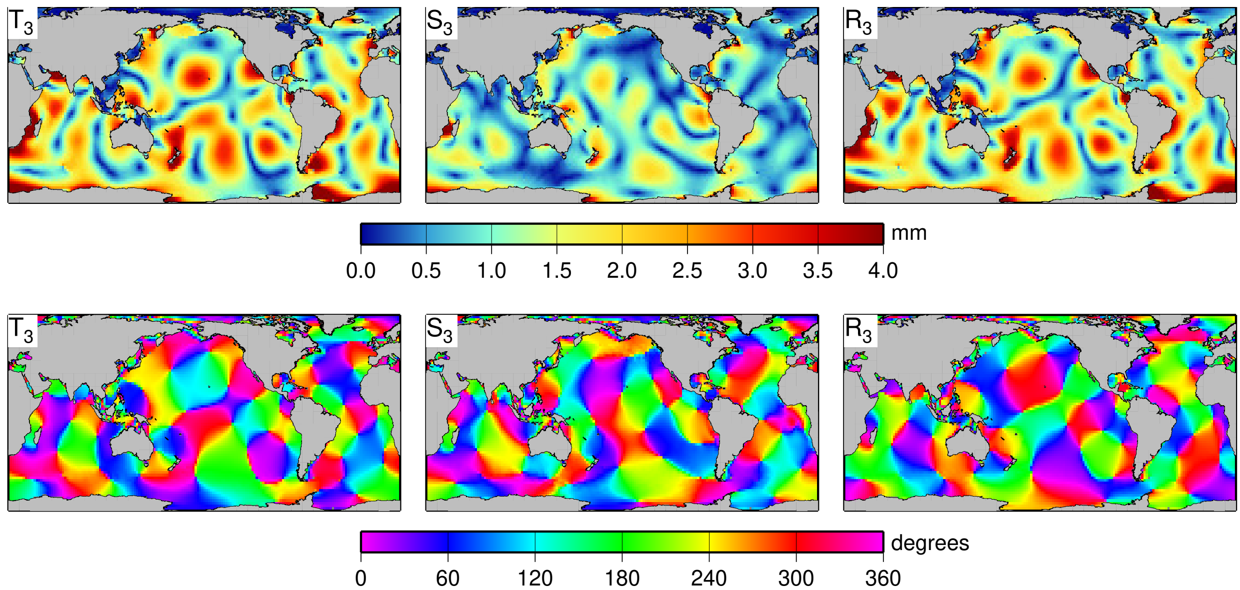

FIG. 6. Modeled terdiurnal radiational tides: the ocean's response to the air pressure tides of Figure 2. Top row displays amplitudes; bottom row displays Greenwich phase lags.

Results are shown in Figure 6. As expected, in light of the forcing, the two sideline tides are larger than the central S_3 tide. Most striking is the different character between forcing and response: the response has little indication of an isostatic response to predominantly mid-latitude forcing, but it is instead a dynamic response with excited higher wavenumbers throughout the globe, including around Antarctica where the air-tide forcing is minimal.

The spatial patterns of T_3 and R_3 amplitudes are quite similar, as is expected from the similar forcing. Their phases, again like the forcing, are opposite. For example, the high-tide region in the central North Pacific has T_3 phase lags around 120°, but R_3 phase lags around 300°.

Like the atmospheric tides analyzed in Section 3, the constituents of Figure 6 can be usefully combined into a single seasonally varying terdiurnal ocean tide. The resulting amplitudes are shown in Figure 7, evaluated when the solar longitude takes values h = 0°, 90°, 180°, 270°. Reflecting the air-tide forcing (Figure 3), the radiational ocean tide is largest during the two solstice seasons and has only small amplitudes during the equinox seasons. During a solstice, T_3 and R_3 combine to form amplitudes larger than either individual constituent—compare color scales in Figures 6 and 7. Similarly, the ocean tide is larger during the winter of each hemisphere. The

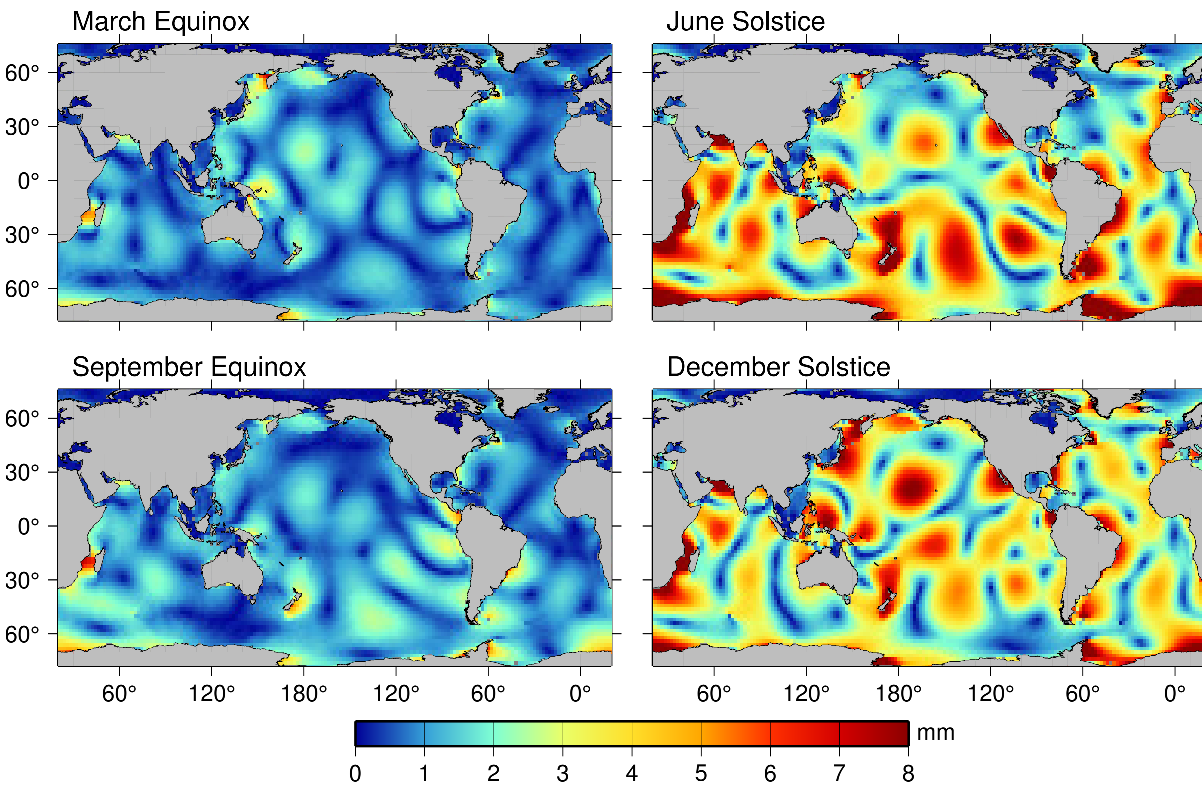

FIG. 7. Amplitudes of the modeled terdiurnal radiational tide, treated as a seasonally-varying single constituent, from a combination of the three waves T_3, S_3, and R_3 shown in Figure 6. As with the forcing atmospheric tide (Figure 3), the ocean tide is largest during solstice seasons with much smaller amplitudes during both equinoxes.

winter enhancement is especially pronounced off the east coast of the United States and along the western boundary of the North Pacific.

a. In situ comparisons

As discussed previously, many of the tide gauges shown in Figure 4 measure a combination of radiational and nonlinear tides. In contrast, the open-ocean bottom pressure stations of Figure 5 appear to measure mostly radiational tides. The latter can thus more easily be used as a "ground truth" dataset for assessing the ocean tides of Figure 6, with the understanding that a significant part of any discrepancy between observations and model must also arise from errors in the air-tide forcing (which is itself assessed in Appendix A).

Because the bottom pressure measurements record the sum of ocean and atmospheric tides, we have added the ERA5 air tides to the model results of Figure 6. The combined model amplitudes

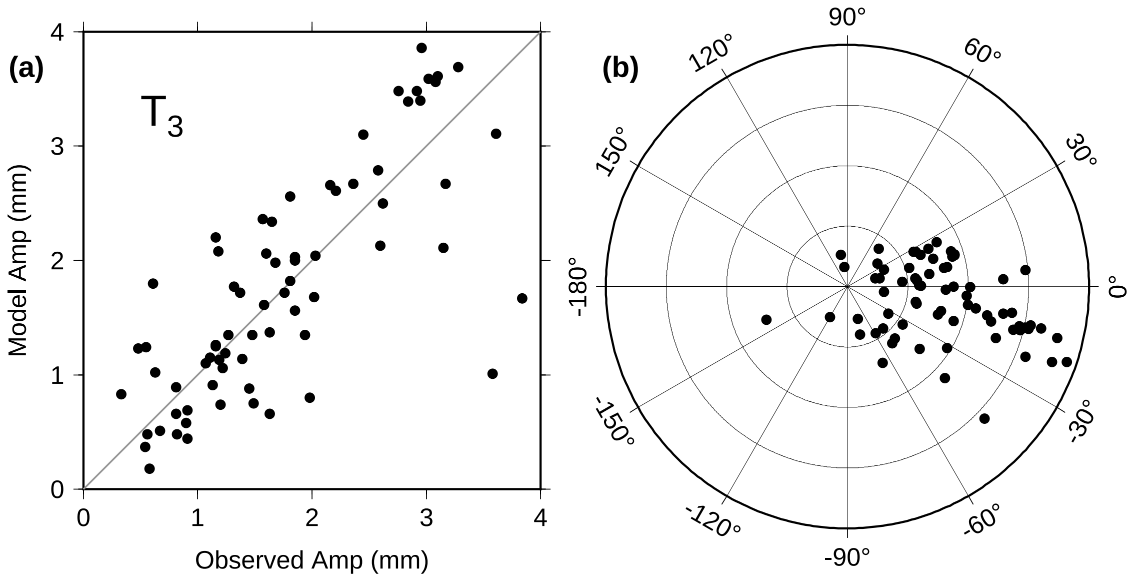

FIG. 8. Comparison of modeled and observed T_3 ocean + air tide, in (a) amplitude and (b) phase lag, with observed amplitudes along the radial axis and with phase differences taken in the sense model-minus-observed. Amplitude axis ticks are 1 mm in both panels. The *in situ* observed data are here the 71 bottom-pressure stations analyzed in Figure 5.

and phase lags for T_3 are compared against the bottom pressure tides in Figure 8. (Results for other waves are similar in character.) The RMS of the complex differences is 0.68 mm, while the RMS signal (from the bottom pressures) is 1.40 mm. The results are encouraging, but they obviously leave room for improvement as the scatter is fairly large, suggesting errors in model ocean tides or air tides or both (and also possible small SP_3 contamination in a few of the bottom-pressure stations). The phase differences (panel b) show a slight tendency to fall around −20°. Such a phase bias must arise from the ocean modeling, since the model air tides show no similar phase bias (Figure A2).

The two worst outlier points in Figure 8 (lower right points in panel (a)) are both from the Drake Passage. These are high-quality stations (Tracey et al. 2013), each four years long and with good year-to-year agreement in the terdiurnal constants. This suggests our model solution, which already displays relatively large amplitudes around Antarctica, may nonetheless still be too small there.

6. Two applications

We present two applications where it is useful to distinguish terdiurnal radiational tides in the S_3 group from possible nonlinear compound tides in the same group. By happenstance both applications are from near the Ross Ice Shelf, but the first example could have been found in many other regions.

a. Differences in nodal modulations

This example stems from work (Ray et al. 2021) on the tides at Cape Roberts, a station maintained by Land Information New Zealand on the coast of Antarctica not far from the Ross Ice Shelf front (77°02′S, 163°11′E). A large suite of tidal constants was estimated from hourly water-level data collected over the period 1990–2018. Results were checked by examining the spectrum of tidal residuals computed from a continuous span of data covering the shorter interval 2006–2008. The residual spectrum in the terdiurnal band, shown in Figure 9b, revealed a small peak near S_3 that persistently resisted attempts to eliminate it.

Panel (b) was based on solving for the three constituents S_3, SP_3, and SK_3 in the S_3 group. The latter included the strong 18.6-y nodal modulation, equivalent to the modulation in the diurnal K_1, (12% in amplitude and 9° in phase). It was eventually realized that terdiurnal radiational tides, not nonlinear tides, were acting at Cape Roberts. Solving for the triplet S_3, T_3, R_3, the latter with no nodal modulation, resulted in the residual spectrum shown in Figure 9c, with no residual peak.

In retrospect, the presence of terdiurnal radiational tides at Cape Roberts should have been clear from the tell-tale characteristics discussed above, most notably from comparable amplitudes of T_3 and R_3 (13.1 and 13.2 mm, respectively) and nearly opposing phase lags (93° and 296°, respectively). Moreover, these two constituents are larger than all other constituents in the terdiurnal band (Ray et al. 2021, Table S1), which is another indicator of radiational, rather than nonlinear, tides.

For such a long time series, one can, of course, solve for individual spectral lines at 1 cycle per 18.6 y resolution, and thereby determine separately SK_3 and its nodal sideline. Amin (1976) computed a similar high-resolution inversion for the tide gauge at Southend (U.K.), although not for S_3. For the main SK_3 line and its nodal sideline, we determined amplitudes of 13.20 ± 0.26 mm and 0.58 ± 0.26 mm, respectively. Because it is barely twice its standard error, the amplitude

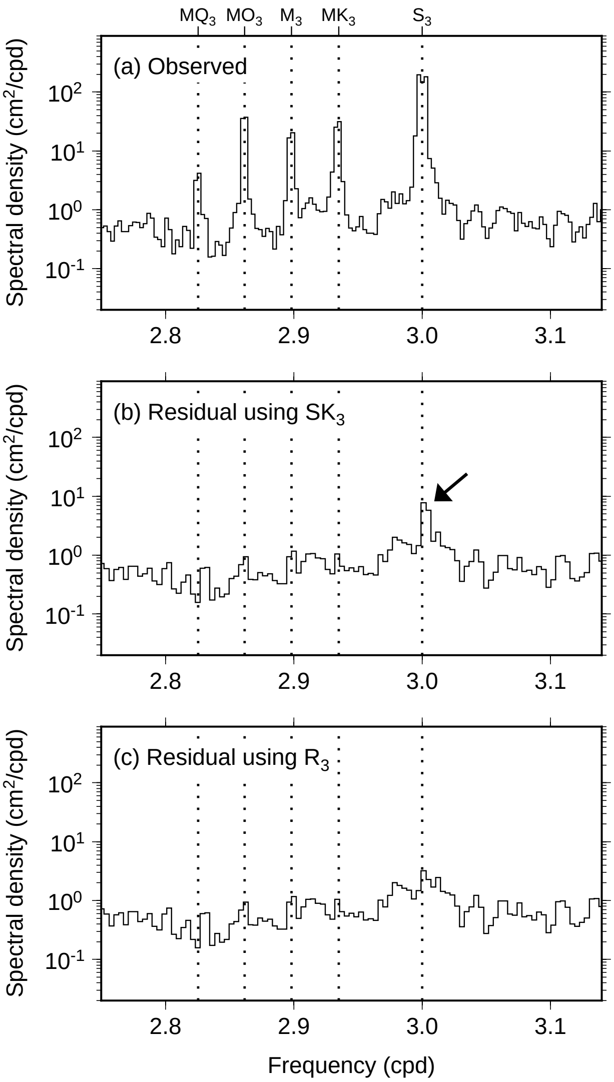

FIG. 9. Terdiurnal spectrum at Cape Roberts, Antarctica, from water levels measured during 2006–2008. (a) Observed spectrum. Largest tidal constituents (or tidal groups) are marked by dotted lines, labeled at top. (b) Spectrum of tidal residuals, after estimating and removing tides over the 1990–2018 time interval. The S_3 group comprised S_3, SK_3 and SP_3. (c) Spectrum of tidal residuals, when the S_3 group comprised S_3, T_3 and R_3. The assumed 18.6-y nodal modulation of SK_3 leaves a small residual peak (marked by arrow), whereas the lack of nodal modulation in R_3 eliminates it.

estimate of the nodal line is biased high. According to Munk and Cartwright (1966, Appendix B), the mean bias[2] in this case is approximately 30%; a corrected amplitude estimate is 0.45 mm. The ratio 0.45/13.20 = 0.034 whereas the theoretical ratio of the two lines is 0.136 (Cartwright

[2]There is a misprint in Eq (B6) of Munk and Cartwright (1966).

and Edden 1973). Thus, the observed nodal modulation is much smaller than expected if the constituent were truly the nonlinear SK_3. This is then separate evidence that the line is mostly R_3.

b. Nonlinear versus radiational tides near Ross Ice Shelf

Over the past several years, as high-rate geodetic instruments have been deployed across the Antarctic ice shelves, the importance of tidal interactions between ocean and ice has become apparent (e.g., Padman et al. 2018). The appearance of nonlinear compound tides in horizontal and/or vertical ice motion can arise from the ocean alone or from the ice's nonlinear flexure response to the ocean tide. Simultaneous ocean and ice measurements are therefore especially valuable for understanding and modeling of ice shelf mechanics.

Recently Begeman et al. (2020) collected pressure measurements beneath the southern Ross Ice Shelf through a borehole located within the grounding zone. A series of GPS measurements have also been collected on the ice surface. The subsurface pressures indicated energy within the S_3 group, but the time series duration (54 days) was too short to distinguish among the different constituents within the group.

The GPS measurements at the surface, however, are longer. Station GZ19 sits on the grounding zone of the ice shelf (Begeman et al. 2020, their Figure 1b), very near the borehole. High-rate (5-min) GPS solutions for GZ19 have been computed by Blewitt et al. (2018) for the period January 2015 to May 2016. Using these GPS solutions, we have estimated the (vertical) tides, including those in the terdiurnal band.[3] A selection of the estimated constituents is given in Table 2. Tide coefficients at GZ19 were also determined by Begeman et al., but from a slightly shorter time series; these are reproduced in the table. Comparisons with our coefficients are reasonably good, although differences often exceed quoted uncertainties. Comparison is poor, however, for one constituent: SK_3 (or R_3), where their amplitude is an order of magnitude smaller.

Based on our estimated amplitudes and phase lags of the three lines in the S_3 group, and in light of our foregoing discussions, we are led to conclude that the two annual sidelines of S_3 at station GZ19 are predominantly the linear radiational tides T_3 and R_3 and not the nonlinear compound tides SK_3 and SP_3. They are of comparable amplitudes (13.0 and 13.7 mm) and approximately out of phase (160° different). They are also significantly larger than all other lines in the terdiurnal

[3] Before tidal estimation, we discarded GPS position estimates with uncertainties exceeding 7 cm, which entailed approximately 4% of the data, and we removed a large vertical trend, estimated at -367 ± 11 mm/y.

TABLE 2. Selected ocean tides at GPS station GZ19 (84°20.1′S, 163°36.7′W)

		This paper			Begeman et al. (2020	
Tide	Frequency (°/h)	H	G	σ	H	G
O_1	13.943036	141.8	191.1	2.1	138 ± 1	189.1 ± 0.4
K_1	15.041069	171.4	207.0	2.1	162 ± 1	206.5 ± 0.4
N_2	28.439730	49.4	142.4	0.7	47.7 ± 0.6	140.2 ± 0.8
M_2	28.984104	36.1	233.6	0.9	33.7 ± 0.6	233 ± 1
S_2	30.000000	53.2	171.7	0.9	49.3 ± 0.7	172.3 ± 0.8
NO_3	42.382765	2.3	88.3	0.9	–	–
MO_3	42.927140	4.9	131.4	0.9	5 ± 1	153 ± 14
M_3	43.476156	4.6	133.0	0.8	–	–
SO_3	43.943036	0.1	318.8	1.0	–	–
MK_3	44.025173	2.9	176.8	0.9	3 ± 1	182 ± 27
T_3	44.958931	13.0	241.2	0.9	–	–
S_3	45.000000	7.5	326.9	1.0	–	–
R_3 / SK_3	45.041069	13.7	81.6	1.0	1 ± 1	343 ± 5

Amplitudes H in mm, Greenwich phase lags G in degrees, standard errors σ in mm. On the final row, we report values for R_3, whereas Begeman et al. (2020) reported SK_3.

band. Admittedly, in this area MK_3 may be anomalously small owing to the anomalously small M_2, but other nonlinear combinations would be expected to approach the amplitude of SK_3 if nonlinearity is actually present. Some nonlinearity, of course, may well be present (MO_3 is almost 5 mm), but the two sidelines of S_3 are likely predominantly linear.

In their analysis of the grounding zone tides, Begeman et al. (2020) understandably assumed that SK_3 was nonlinear, and they explored some of the consequences of a large nonlinear tide for understanding the regional ice-ocean interaction ('large' at least in their power spectrum if not in their tidal estimation). For example, they rightly argue for the importance of studying spatial variation in nonlinear tides, which can place constraints on effective drag coefficients with the ice. Some of their discussion, however, is necessarily impacted if SK_3 is actually a linear constituent. Begeman et al. also noticed that a "decrease in nonlinear tide amplitudes from the freely floating ice shelf to the grounding zone was unexpected; typically nonlinear tides increase in amplitude in shallow water." This quandary can be explained if the constituent is a linear radiational wave, for then it would likely decrease in the grounding zone in the same manner that linear waves in the semidiurnal and diurnal bands are observed to decrease.

Additional evidence for radiational tides at both Cape Roberts and GZ19 is the model ocean tide of Figure 6, which displays some of its largest amplitudes along the coast of Antarctica, especially for constituent R_3. This is the case even though the forcing air pressures are small throughout those southern latitudes (Figure 2), which emphasizes the highly dynamic and global response of the ocean to the air-pressure loading (note similarly large R_3 amplitudes near southern Greenland in Figure 6 where the local air-tide forcing is also small).

The ice-cavity pressure measurements of Begeman et al. (2020) were collected from mid-January to mid-March of 2015, during which, according to our model (Figure 7), the terdiurnal radiational tide in the Ross Sea had an initial amplitude of about 1 cm, falling by mid-March to nearly zero. Begeman et al. reported an amplitude of 0.5 ± 0.6 cm, where the large error estimate presumably reflected large residual variance in the terdiurnal band.

7. Summary

Tide gauge data commonly contain energy in a narrow band of frequencies centered at 3 cpd, the frequency of the constituent S_3. In analysis of a short time series, the peak is typically assigned to the SK_3 nonlinear compound tide, but longer time series often reveal separate peaks at the frequencies of SK_3, SP_3, and S_3. As we have shown, when tidal estimation finds SK_3 and SP_3 amplitudes of comparable magnitude and when both are large relative to other terdiurnal constituents, it is probably because they are not compound tides at all, but rather radiational tides, which arise from pressure loading of the ocean by atmospheric tides. The forcing mechanism is similar to that causing the radiational tide S_1 (Ray and Egbert 2004) and the (usually small) radiational component of S_2 (Zetler 1971; Arbic 2005; Dobslaw and Thomas 2005). In these cases, we prefer to label the S_3 sidelines T_3 and R_3, in analogy with Kelvin's labels for the annual sidelines of the semidiurnal S_2, even though the physical mechanisms causing the modulations are totally different.

The unusual terdiurnal atmospheric tide nearly vanishes during times near the spring and autumn equinoxes. With its forcing removed, the radiational ocean tide is similarly suppressed near the equinoxes. In each hemisphere the tide is slightly larger in winter than in summer. These seasonal characteristics are one indicator that radiational tides, rather than nonlinear tides, are in play. The other indicator, as noted, are amplitudes larger than that of MK_3, which in most places is expected to be the largest nonlinear terdiurnal constituent.

Terdiurnal radiational tides, like typical constituents of the terdiurnal band, nonlinear or not, are small. Throughout most of the open ocean they are only a few mm, and none of our coastal tide-gauge amplitudes exceeded 4 cm (Figure 4). In light of these small amplitudes, our study may be criticized as much ado about very little. If judged merely in terms of obtaining improved tidal predictions, we agree. Even the residual peak seen at Cape Roberts (Figure 9), arising from a misattributed nodal modulation, amounts to a prediction error of only about 3 mm^2 in variance. Yet even tiny tides can reveal important information about the ocean, its forcing, or its response. Knowing whether a constituent is forced by atmospheric tides or by nonlinearity (or both) can critically affect physical interpretation of measurements (e.g., Begeman et al. 2020), no matter how small the signal.

Acknowledgments. We thank Carolyn Branecky Begeman for useful discussions and Henryk Dobslaw for useful comments. This work was supported by the National Aeronautics and Space Administration through the Ocean Surface Topography and Sentinel-6 programs.

Data availability statement. The ECMWF ERA5 pressure data are available from the Copernicus Climate Change Service `https://cds.climate.copernicus.eu`. The MERRA2 pressure data are available from `https://gmao.gsfc.nasa.gov/reanalysis/MERRA-2`. The ISD meteorological station data are available from the NOAA National Centers for Environmental Information `https://www.ncei.noaa.gov/products/land-based-station/integrated-surface-database`. The GESLA2 tide gauge data are at `https://gesla.org`.

APPENDIX A

Assessment of Reanalysis Air Tides

The reanalysis air tides (Figure 2) are fundamental to the analysis here and of our understanding of the resulting ocean response. It is therefore useful to have an independent assessment of their accuracy. We also need to determine which of the two reanalysis products discussed above is to be preferred for the ocean modeling work. This appendix describes an assessment of the reanalysis tide products based on "ground truth" air tide estimates obtained at a selected set of meteorological stations. Similar exercises have previously addressed model accuracies of diurnal and semidiurnal atmospheric tides (e.g., Ray 2001; Covey et al. 2014). Tidal estimates from time series of barometer measurements, of course, are far from perfect and have their own possible error sources.

We computed tide estimates at a set of 89 barometer stations, selected specifically to assess the air-tide models over ocean regions. All are stations located on small islands, with somewhat greater emphasis given to lower latitudes where tidal amplitudes are largest. Time series have been collected from a variety of sources. Most are taken from the Integrated Surface Database (Smith et al. 2011) as well as the earlier Surface Airway Hourly Observations (TD3280) from the National Climatic Data Center. Some of the highest quality data are from the NOAA Center for Operational Oceanographic Products and Services (CO-OPS) which distributes meteorological data collected near U.S. tide gauges (including gauges in the Caribbean and Pacific). The time series include hourly, 3-hourly, or mixed sampling, preferentially station pressures or "altimeter setting" pressures; the latter were subsequently converted to station pressure (Pauley 1998). Pressures

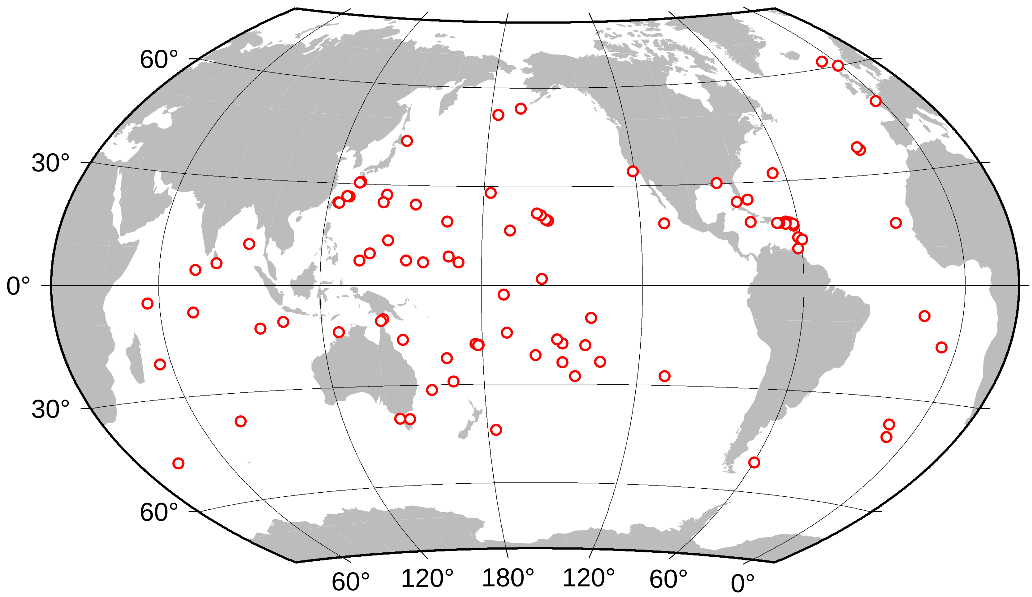

FIG. A1. Island locations where atmospheric tidal constants have been estimated from long time series of barometer measurements. These data are used in Table A1.

reduced to sea level were used only for low-elevation stations, because it is known that reduction methods can distort tidal signals (Mass et al. 1991). The shortest time series was 8 years, the longest 38 years, with the median at 15 years. The station distribution is shown in Figure A1.

Tidal estimates have been computed using standard least-squares methods, generally for 17 constituents, including annual and semiannual. Solutions were also computed on a year-by-year basis and compared for consistency. This sometimes revealed, for example, timing or other errors, either jumps or even slow drifts, and several time series were discarded based on these tests. While our focus is the terdiurnal constituents, we also include some results for the semidiurnal S_2; being of much greater signal it adds useful information to the assessments.

Figure A2 shows amplitude and phase comparisons for the ERA5 tides at all 89 stations, for the three terdiurnals plus S_2. For the latter, the signal-to-noise ratio is clearly best, with the points more tightly clustered around the amplitude diagonal line and the zero phase difference axis. The points are scattered more erratically for the small S_3 constituent, in both amplitude and phase.

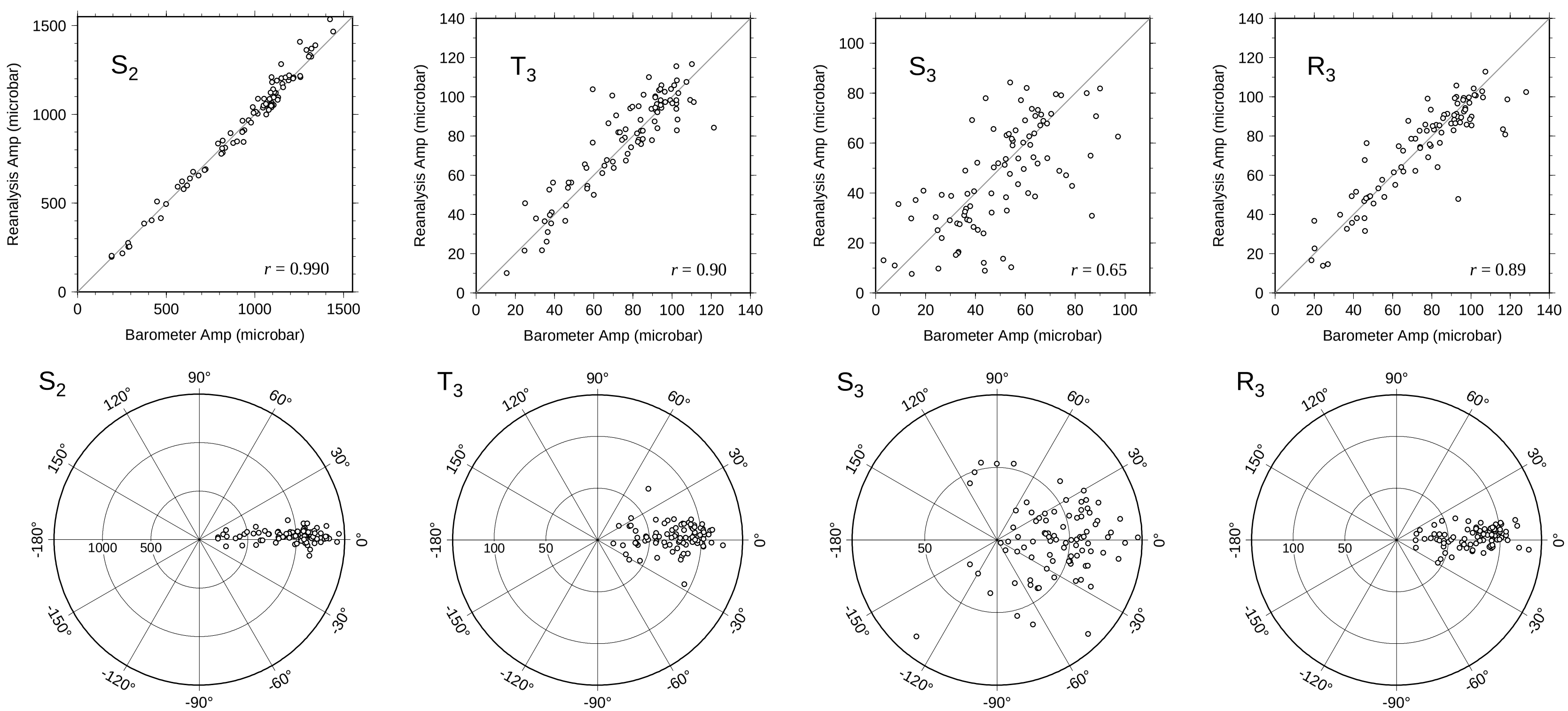

Fɪɢ. A2. Comparisons of ERA5 surface-pressure amplitudes (top) and phases (bottom) with 89 station-based tidal constants. Model-minus-station phase differences are shown in the polar diagrams as a function of station amplitudes (in μb).

TABLE A1. Comparisons of reanalysis air tides with measurements at 89 barometric stations.

Tide	RMS signal	Reanalysis	RMS diff.	Amplitudes Slope	r	Phases $\overline{\Delta\phi}$	s.d.$(\Delta\phi)$
S_2	703	ERA5	59	1.007 ± 0.011	0.990	2.4°	3.8°
		MERRA2	115	1.053 ± 0.012	0.986	−7.2°	3.6°
T_3	56	ERA5	12	1.028 ± 0.034	0.897	2.3°	10.0°
		MERRA2	14	0.921 ± 0.028	0.877	5.1°	11.2°
S_3	38	ERA5	24	0.946 ± 0.066	0.653	−1.8°	41.7°
		MERRA2	34	0.829 ± 0.104	0.313	−17.2°	65.7°
R_3	57	ERA5	10	0.979 ± 0.031	0.893	2.2°	7.2°
		MERRA2	13	0.953 ± 0.032	0.883	3.8°	9.7°

RMS units in μb. Slope is from orthogonal regression assuming comparable errors in both variables. r is Pearson correlation coefficient. Statistics of phase differences $\Delta\phi$ are weighted by amplitude.

Statistical comparisons are summarized in Table A1 for both ERA5 and MERRA2. Tabulated are: RMS differences for the 89 stations; amplitude ratios, computed from an orthogonal regression fit of the reanalysis amplitudes versus station amplitudes; the amplitude correlation coefficients; the mean phase differences for the 89 stations, weighted by station amplitude (as large phase differences are of little concern if amplitudes are small); and the standard deviation of the phase differences, a measure of the phase scatter shown in the bottom panels of Figure A2.

Table A1 shows clearly that ERA5 agrees better than MERRA2 with the station tidal estimates. The RMS differences are smaller for all four constituents, the amplitude correlations are larger, and the mean phase differences are smaller. The regression slopes suggest possible systematic errors in MERRA2 amplitudes, most convincingly for S_2 for which the slope bias of 5.3% exceeds four times the uncertainty.

Neither Table A1 nor the diagrams of Figure A2 give any suggestion of systematic errors in the ERA5 tides. For this reason, we adopted them for forcing the ocean model in Section 5.

References

Akmaev, R. A., 2001: Seasonal variations of the terdiurnal tide in the mesosphere and lower thermosphere: a model study. *Geophys. Res. Lett.*, **28**, 3817–3820.

Amin, M., 1976: The fine resolution of tidal harmonics. *Geophys. J. R. astr. Soc.*, **44**, 293–310.

Arbic, B. K., 2005: Atmospheric forcing of the oceanic semidiurnal tide. *Geophys. Res. Lett.*, **32 (2)**, L02 610, https://doi.org/10.1029/2004GL021668.

Begeman, C. B., S. Tulaczyk, L. Padman, M. King, M. R. Sieffried, T. O. Hodson, and H. A. Fricker, 2020: Tidal pressurization of the ocean cavity near an Antarctic ice shelf grounding line. *J. Geophys. Res.: Oceans*, **125**, e2019JC015 562, https://doi.org/10.1029/2019JC015562.

Blewitt, G., W. C. Hammond, and C. Kreemer, 2018: Harnessing the GPS data explosion for interdisciplinary science. *EOS*, **99**, https://doi.org/10.1029/2018EO104623.

Cartwright, D. E., and A. C. Edden, 1973: Corrected tables of tidal harmonics. *Geophys. J. R. astr. Soc.*, **33**, 253–264.

Covey, C., A. Dai, R. S. Lindzen, and D. R. Marsh, 2014: Atmospheric tides in the latest generation of climate models. *J. Atmos. Sci.*, **71**, 1905–1913, https://doi.org/10.1175/JAS-D-13-0358.1.

Dobslaw, H., and M. Thomas, 2005: Atmospheric induced oceanic tides from ECMWF forecasts. *Geophys. Res. Lett.*, **32**, L10615, https://doi.org/10.1029/2005GL022990.

Egbert, G. D., and S. Y. Erofeeva, 2002: Efficient inverse modeling of barotropic ocean tides. *J. Atmos. Oceanic Tech.*, **19**, 183–204.

Gelaro, R., and Coauthors, 2017: The modern-era retrospective analysis for research and applications, version 2 (MERRA-2). *J. Climate*, **30**, 5419–5454, https://doi.org/10.1175/JCLI-D-16-0758.1.

Godin, G., 1986: Is the abnormal response of the tide at the frequency of S_2 really due to radiational effect? *Cont. Shelf Res.*, **6**, 615–625.

Hann, J., 1918: Untersuchungen über die tägliche Oszillation des Barometers: III. Die dritteltägige Luftdruckschwankung. *Denkschr. Akad. Wiss. Wien*, **95**, 1–64.

Hersbach, H., and Coauthors, 2020: The ERA5 global reanalysis. *Quart. J. Royal Met. Soc.*, **146**, 1999–2049, https://doi.org/10.1002/qj.3803.

Lyard, F., F. Lefevre, T. Letellier, and O. Francis, 2006: Modelling the global ocean tides: modern insights from FES2004. *Ocean Dynam.*, **56**, 394–415, https://doi.org/10.1007/s10236-006-0086-x.

Mass, C. F., W. J. Steenburgh, and D. M. Schultz, 1991: Diurnal surface-pressure variations over the continental United States and the influence of sea level reduction. *Mon. Wea. Rev.*, **119**, 2814–2830.

Meeus, J., 1998: *Astronomical Algorithms*. 2nd ed., Willmann-Bell, Richmond.

Moudden, Y., and J. M. Forbes, 2013: A decade-long climatology of terdiurnal tides using TIMED/SABER observations. *J. Geophys. Res.: Space Phys.*, **118**, 4534–4550, https://doi.org/10.1002/jgra.50273.

Munk, W. H., and D. E. Cartwright, 1966: Tidal spectroscopy and prediction. *Phil. Trans. Royal Soc.*, **A259**, 533–581.

Padman, L., M. R. Siegfried, and H. A. Fricker, 2018: Ocean tide influences on the Antarctic and Greenland ice sheets. *Rev. Geophys.*, **56**, 142–184, https://doi.org/10.1002/2016RG000546.

Pauley, P. M., 1998: An example of uncertainty in sea level pressure reduction. *Wea. Forecasting*, **13**, 833–850.

Pugh, D. T., and P. L. Woodworth, 2014: *Sea Level Science: Understanding Tides, Surges, Tsunamis and Mean Sea-Level Changes*. Cambridge Univ. Press, Cambridge.

Ray, R. D., 2001: Comparisons of global analyses and station observations of the S_2 barometric tide. *J. Atmos. Solar-Terr. Phys.*, **63**, 1085–1097.

Ray, R. D., 2013: Precise comparisons of bottom-pressure and altimetric ocean tides. *J. Geophys. Res.: Oceans*, **118**, 4570–4584, https://doi.org/10.1002/jgrc.20336.

Ray, R. D., and G. D. Egbert, 2004: The global S_1 tide. *J. Phys. Oceanogr.*, **34**, 1922–1935.

Ray, R. D., K. M. Larson, and B. J. Haines, 2021: New determinations of tides on the north-western Ross Ice Shelf. *Antarc. Sci.*, **33**, 89–102, https://doi.org/10.1017/S0954102020000498.

Ray, R. D., and S. Poulose, 2005: Terdiurnal surface-pressure oscillations over the continental United States. *Mon. Wea. Rev.*, **133**, 2526–2534.

Schureman, P., 1940: Manual of harmonic analysis and prediction of tides. Spec. Publ. 98, U.S. Coast & Geodetic Survey, Washington. 317 pp.

Siebert, M., 1961: Atmospheric tides. *Adv. Geophys.*, **7**, 105–187.

Smith, A., N. Lott, and R. Vose, 2011: The Integrated Surface Database: Recent developments and partnerships. *Bull. Am. Meteorol. Soc.*, **92**, 704–708, https://doi.org/10.1175/2011BAMS3015.1.

Smith, A. K., 2000: Structure of the terdiurnal tide at 95 km. *Geophys. Res. Lett.*, **27**, 177–180.

Thayaparan, T., 1997: The terdiurnal tide in the mesosphere and lower thermosphere over London, Canada (43°N, 81°W). *J. Geophys. Res.*, **102**, 21 695–21 708.

Tracey, K. L., K. A. Donohue, D. R. Watts, and T. Chereskin, 2013: cDrake CPIES data report. GSO Tech. Report 2013-01, Graduate School of Oceanography, Univ. Rhode Island, Narragansett, 80 pp.

van den Dool, H. M., S. Saha, J. Schemm, and J. Huang, 1997: A temporal interpolation method to obtain hourly atmospheric surface pressure tides in Reanalysis 1979–1995. *J. Geophys. Res.*, **102**, 22 013–22 024.

Woodworth, P. L., J. R. Hunter, M. Marcos, P. Caldwell, M. Menéndez, and I. Haigh, 2017: Towards a global higher-frequency sea level dataset. *Geosci. Data J.*, **3**, 50–59, https://doi.org/10.1002/gdj3.42.

Zetler, B. D., 1971: Radiational ocean tides along the coasts of the United States. *J. Phys. Oceanogr.*, **1**, 34–38.